Applied Thermal Engineering 132 (2018) 613–623

Contents lists available at ScienceDirect

Applied Thermal Engineering

journal homepage: www.elsevier.com/locate/apthermeng

Research Paper

Modeling counter-flow particle heat exchangers for two-step solar thermochemical syngas production

Christoph P. Falter [a,*], Robert Pitz-Paal [b]

[a] Bauhaus Luftfahrt, Willy-Messerschmitt-Straße 1, 82024 Taufkirchen, Germany
[b] DLR, Institute of Solar Research, Linder Höhe, 51147 Köln, Germany

HIGHLIGHTS

- A generic model of a counter-flow particle heat exchanger is presented.
- Different geometries and process conditions are investigated.
- Heat diffusion in the particle beds can limit the performance of the heat exchanger.
- Mixing of the particle beds significantly enhances the heat exchanger performance.
- Optimal values for geometry and process variables are found in a parameter study.

GRAPHICAL ABSTRACT

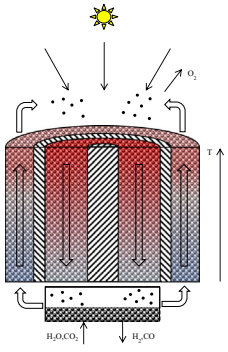

ARTICLE INFO

Article history:
Received 30 January 2017
Revised 13 November 2017
Accepted 23 December 2017
Available online 26 December 2017

Keywords:
Solar fuel
Redox cycle
Particles
Heat recovery
Model

ABSTRACT

Particle reactor concepts have been suggested for the implementation of two-step solar thermochemical redox cycles due to several inherent advantages such as new heat exchanger concepts, flexibility of the reactor design, fast reaction kinetics due to high surface area of the reactive medium, and resistivity to thermal shocks. Further, heat recuperation from the solid phase has been shown to be crucial for the achievement of high efficiencies using reactive material undergoing nonstoichiometric redox reactions at different temperature levels. It is therefore of interest to investigate the potential for heat recuperation from the solid phase of the reactive material for reactor concepts based on particles. We present a model of a generic double-walled heat exchanger for the counter-flow of reduced and oxidized particles, where heat is transferred from the hot to the cold particles through a separating wall, which prevents mixing of the atmospheres. The upper and lower bound for the performance of the heat exchanger of perfectly mixed und unmixed beds are evaluated. Heat transfer in the particle beds and between the beds and the separating wall is described with published models, and the results are compared with experimental data from the literature. A parameter study is performed on a chosen system implementation with a size of recent laboratory demonstrations, where entry temperatures, geometries and residence times of the particles in the heat exchanger are varied. It is found that heat exchanger effectiveness is maximized for higher entry temperatures and for optimum values of the geometry and residence time balancing enhanced heat transfer between the particle beds and increased losses to the environment. Heat exchanger effectiveness reaches values of over 50% for unmixed beds and over 80% for perfectly mixed beds for an optimal choice of parameters. Effectiveness can be significantly enhanced through radial mixing of the beds, as the main limitation of heat transfer through the beds is reduced.

* Corresponding author.
E-mail addresses: christoph.falter@bauhaus-luftfahrt.net (C.P. Falter), robert.pitz-paal@dlr.de (R. Pitz-Paal).

https://doi.org/10.1016/j.applthermaleng.2017.12.087
1359-4311/

Nomenclature

A	area [m^2]
a	diameter of contact surface area between particle and wall in case particles are not spherical [m^2]
C_f	form factor of particles [–]
c_p	heat capacity at constant pressure [J mol^{-1} K^{-1}]
D	diameter of cylinder [m]
d	particle diameter [m]
h	height of cylinder, length of heat exchanger [m]
k	thermal conductivity with respect to thermal conductivity of gaseous phase [–]
L	length of wall [m]
l	modified mean free path [m]
M	molecular mass [kg mol^{-1}]
m	index of numerical layers in axial direction [–]
$\dot{m}$	mass flow rate
Nu	Nusselt number [–]
p	pressure [Pa]
Pr	Prandtl number [–]
Ra	Rayleigh number [–]
T	temperature [K]
t	time [s]
Δt^{num}	residence time in numerical layer in particle bed [s]
v	velocity [m/s]

Greek letters

α	heat transfer coefficient [W m^{-1} K^{-1}]
β_R	Rossland mean attenuation coefficient
γ	accommodation coefficient [–]
δ	roughness factor of particles [m]
ϵ	emissivity [–]
ε	effectiveness [–]
η_{vis}	dynamic viscosity [Pa s]
Λ	mean free path [m]
λ	thermal conductivity [W m^{-1} K^{-1}]
ρ	density [kg m^{-3}]
σ	Stefan-Boltzmann constant [W m^{-2} K^{-4}]
Φ_A	plate surface coverage factor by particles [–]
φ	porosity [–]
ψ	flatness coefficient of particles [–]

Symbols

$\mathcal{R}$	ideal gas constant [J mol^{-1} K^{-1}]

Subscripts

0	surroundings
bed	particle bed
c	core
conv	convection
crit	critical time at which $\alpha_{ws} = \alpha_{sb}$
dir	direct contact of particle and wall
f	fluid
G	gas phase
H	higher entry temperature into heat exchanger, equals reduction temperature
L	lower entry temperature into heat exchanger, equals oxidation temperature
p	particle
rad	radiation
s	reactive material
sb	in particle bed
wp	wall-particle
ws	wall-surface of particle bed

Heat exchanger concepts based on the counter-flow of solid reactive particles are thus shown to have a high potential and the presented computational model is a valuable tool for the evaluation of their performance and guidance for their design.

1. Introduction

Liquid hydrocarbon fuels are ideally suited for transportation applications due to their high specific energy, energy density and because they allow large power densities. However, concerns about their long-term availability and their impact on the climate have led to a search for alternatives, where long-range air travel is likely to rely on liquid hydrocarbon fuels also in the future. The use of solar energy for the production of a renewable fuel, which is at the same time compatible with the infrastructure in use today appears to be a desirable solution to the challenges associated to conventional fuels [1,2]. Many different fuel options based on solar primary energy exist, e.g. biofuels, solar electrochemical fuels, or solar thermochemical fuels. In recent implementations of the solar thermochemical pathway, synthesis gas (a mixture of hydrogen and carbon monoxide) is produced by two-step redox reactions with a metal oxide, where ceria has shown high experimental efficiencies to date [1,3-6] with the recent achievement of above 5% [7]. This value has been achieved in a cavity reactor using ceria in the form of a reticulated porous ceramic without heat recuperation. However, for the achievement of higher efficiencies, the implementation of heat recuperation from the solid and gaseous phase is imperative [8,9]. Different approaches for heat recuperation have been suggested in the literature, e.g. from the solid phase in cylindrical geometries of reactive material with or without inert material for heat exchange [10,11], a counter-flow of hot and cold reactive material in a chamber system for radiation heat exchange [9], by direct contact of particles with a heat exchange medium of similar morphology that can be separated by their different diameters [12], by counter-flow of reduced and oxidized particles in a double-walled geometry [13], from the gaseous phase using reticulated porous alumina in a counter-flow configuration [5,14], or by using the heat in thermochemical energy storage media [15]. In the suggested concepts, the reactive material is usually either in the form of porous structures such as reticulated porous ceramics (RPC) [16] or in the form of particles [13]. Porous structures have enabled robust experimental campaigns, while particles offer certain advantages such as a larger flexibility in the reactor design, high heating rates [17], resistivity to thermal shocks, a high surface-to-volume ratio, sealing between the reaction chambers, or the internal mixing of reactive material aiding thermal diffusion, besides others. The use of particles for solar applications has been

discussed e.g. for CSP plants to raise the temperature of the heat transfer medium towards 1000 °C [18–20] and thus to increase effectiveness of the thermodynamic cycle, for thermochemical syngas production with particles falling through an indirectly heated tube in counter-flow with argon [17], particles moving in counter-flow between the reaction chambers to exchange heat [13], for the dissociation of ZnO-particles in a rotating cavity-receiver [21], for the conversion of a methane flow laden with carbon black particles to carbon and hydrogen [22], for an internally circulating fluidized bed of ferrite particles for syngas production [23], as a heat storage medium providing high-temperature heat in a solar Brayton cycle [15,24], and for CO_2 removal from a gas stream by CaO-carbonation and $CaCO_3$ calcination [25].

So far, the number of publications regarding the performance potential for solid-solid particle heat exchange in solar thermochemical cycles is limited [5,13,14]. Given the potential advantages of solid-solid particle heat exchange, it is of high interest to analyze their performance limits in more detail. In the following, we consider a particle heat exchanger for a two-step ceria redox cycle which, operates between a reduction temperature of 1800 K and an oxidation temperature of 1000 K, where these temperatures are defined to be the inlet temperatures to the heat exchanger. Based on a size that corresponds to recent laboratory experiments of 4 kW solar input power [7], a generic model is presented of a counter-flow particle heat exchanger, where heat is transferred from the hot reduced particles to the cold oxidized particles in a concentric tubular geometry. Upper and lower heat exchanger effectiveness are evaluated based on the assumptions of no mixing and perfect mixing (perpendicular to the particle bed movement) of each of the particle beds with a sensitivity study of the heat exchanger geometry, entry temperatures and residence times. A high potential for heat recuperation is found, which is maximized for specific geometries and residence times of a perfectly mixed bed towards high inlet temperatures.

2. Model description

A particle heat exchanger is modeled for a two-step thermochemical redox cycle (see Fig. 1). Particles from the oxidation chamber are fed to the bottom of the outer tube of the heat exchanger, inducing an upward movement of the packed bed of oxidized particles. When reaching the top, the oxidized particles fall into the annular section of the inner tube of the heat exchanger and are directly irradiated by solar energy. After moving through the heat exchanger, the reduced particles are removed from the bottom and inserted into the oxidation chamber, where they are contacted with H_2O, CO_2, or a mixture thereof, to produce syngas.

The system boundary comprises only the heat exchanger, where the temperatures of the particles entering the heat exchanger are assumed to be the reaction temperatures, i.e. 1800 K for the hot reduced particles and 1000 K for the cold oxidized ones. The heat exchanger consists of a double-walled tube, where the oxidized cold particles are elevated in an outer packed bed and the reduced hot particles are moving in a counter-flow packed bed on the inside. High temperature particle transport could be performed through an elevation mechanism based on a bucket elevator or the Olds elevator [26], which has been demonstrated to work at high temperature and under vacuum pressure [27]. Alternatively, a feeder based on a reciprocating piston with a detention mechanism could be imagined. Other more complicated geometries can be analyzed once the lift mechanism is known. For a detailed design of the particle flow, possible limitations due to interlocking arching (for large particles mechanically interlocking) or cohesive arching (for small particles bonding together) have to be taken into account, which goes beyond the scope of this analysis. As was already observed for RPC metal oxide [28], heat diffusion in the reactive material is a limiting factor for heat exchange. Therefore, to improve the heat exchange, an inert cylindrical centerpiece is added to force the reduced particles into a hollow cylinder, which reduces the bed thickness. In this way, the volume of particles far from the heat exchange surface is minimized and the required length of heat diffusion within the particle bed is reduced.

For the baseline of the model, a size corresponding to recent laboratory experiments with a solar input power of 4 kW is chosen [1,3]. An implementation of the heat exchanger is then defined according to the required mass flow of material and used as the baseline defined below. The following materials and design parameters have been used for the modeling. The heat exchanger wall is a solid domain and made from Inconel 600 at a thickness of 0.003 m. The insulation between the outer wall and the moving bed of oxidized particles is a porous domain made from Al_2O_3 at a thickness of 0.1 m. The separating wall between the moving beds of particles is a solid domain from (non-porous) Al_2O_3 at a thickness of 0.003 m. The separation between the beds provides sealing with respect to evolving gases and should otherwise have a high thermal conductivity to facilitate heat exchange. Non-porous Al_2O_3 is therefore chosen as it is suitable for the process temperatures and provides a seal for the gases. The inner tube at the center of the heat exchanger has a diameter of 0.04 m and is made from porous Al_2O_3 to provide insulation. Alumina was chosen because a successful use with ceria was demonstrated in recent experiments [1,3,7,16]. The chosen diameters of the moving beds fulfill conservation of mass flux and velocity, i.e. the mass flow of oxidized particles is equal to the mass flow of reduced particles. The moving beds of particles are modeled as porous domains. Heat is transferred mainly by radiation and conduction inside of the moving beds, and between the beds and the adjacent domains, where convection has only a minor contribution [29]. In the solid domains, heat is transferred by conduction only. Heat is lost from the reactor walls to the surroundings by convection and radiation. At the top end of the heat exchanger where solar energy is incident on the particles, a fixed temperature is chosen for the reduced particles. The inlet temperature to the heat exchanger at the bottom is assumed to be equal to the oxidation temperature.

2.1. Governing equations

In the following, the governing equations for the description of heat transfer in the computational domains are introduced.

2.1.1. Porous insulation

In the porous insulation, heat is transferred by conduction and radiation. The application of the Rosseland diffusion approximation leads to an overall thermal conductivity, which is comprised of the sum of a radiative and a conductive part. The overall conductivity is then used in the law of Fourier.

$$\rho c_p \frac{\partial T}{\partial t} = \nabla[(\lambda_{\mathrm{Ins,cond}} + \lambda_{\mathrm{Ins,rad}})\nabla T] \tag{1}$$

$$\lambda_{\mathrm{Ins,rad}} = \frac{16\sigma T^3}{\beta_R}, \tag{2}$$

where β_R is the Rosseland mean attenuation coefficient. The Rosseland diffusion approximation has been reported to diverge from the correct solution under anisotropic conditions [30]. Due to the proximity of particles and wall, the anisotropy is expected to be lower than at a solid-fluid boundary. The heat transfer at the boundary of the particle beds is specifically addressed in the model by the

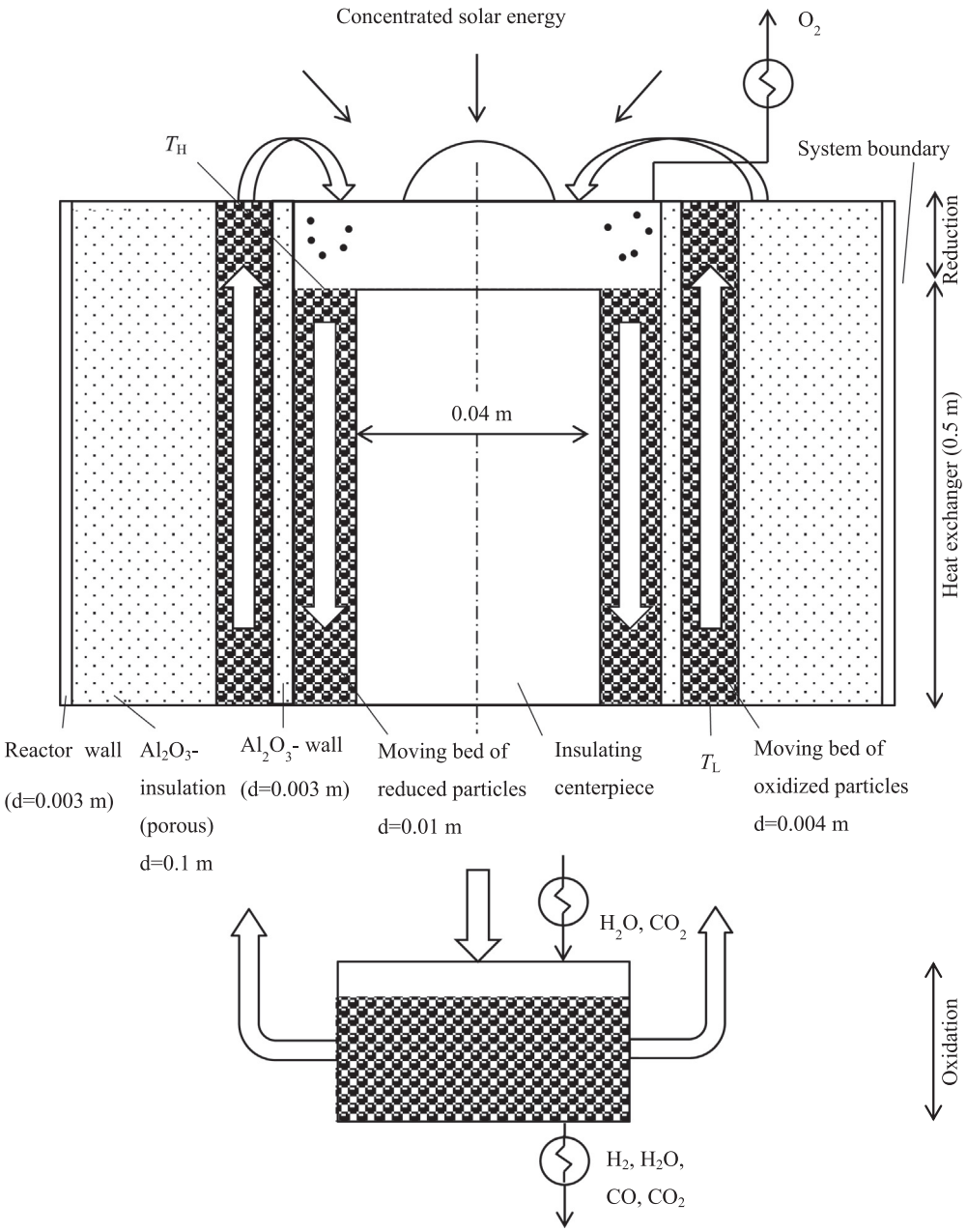

Fig. 1. Schematic of particle heat exchanger model including computational domains and dimensions for baseline case (not to scale).

introduction of a heat transfer coefficient between bed and adjacent wall.

2.1.2. Particle bed domains

For the description of thermal energy transfer between the surrounding walls and the beds of particles, the model proposed by Schlünder [31] is used, which is presented in the following. In the model, an expression for the heat transfer coefficient α is found, which allows the description of the heat flow between the wall and the bed according to

$$\dot{Q}_{\text{wall-bed}} = \alpha A \Delta T. \tag{3}$$

The overall conductivity α for thermal energy transfer between the wall and the adjacent bed of particles is then related to the single conductivities α_{ws} and α_{sb}, describing heat transfer at the boundary of the wall and the particle bed and heat transfer in the particle bed, respectively.

$$\frac{1}{\alpha} = \frac{1}{\alpha_{ws}} + \frac{1}{\alpha_{sb}} \tag{4}$$

The detailed description of the heat transfer coefficients can be found in the Appendix A.

For the description of heat transfer in the particle bed, the model after Zehner, Bauer and Schlünder [32] is used, which gives an expression for the thermal conductivity of the bed λ_{bed}, which can then be used in the law of Fourier. In this model, a representative unit cell of the particle bed is analyzed, which is comprised of a cylindrical core with two opposing particle halves, and a fluid layer surrounding the core. The incorrect assumption of parallel heat flow lines is sought to be corrected by simulating spherical particles with non-spherical particles [32]. The model is used in its more complicated form including the effects of radiation, pressure dependency, and heat transfer through non-spherical particles. A detailed description can be found in the Appendix A.

2.2. Porosity of particle beds

The porosity of fixed particle beds in cylindrical geometries was analyzed by Pushnov [33] who found a functional dependence on the diameter of the cylindrical enclosure D and the particle diameter d.

$$\varphi = \frac{A}{\left(\frac{D}{d}\right)^n} + B \tag{5}$$

with A = 1.0, B = 0.375, and n = 2 for spherical particles [33]. The formula is used here with the diameter D equal to the thickness of the annular rings. Due to the condition of mass conservation, the radial dimensions of the hot and cold particle beds differs, which causes the porosity of the beds to deviate slightly, as well.

2.3. Boundary conditions

Energy is transferred by radiation and convection from the reactor wall to the surroundings, which are assumed to have a temperature of 300 K.

$$\lambda \Delta T|_{\text{wall}\to 0} = \epsilon_{\text{wall}} \sigma (T_{\text{wall}}^4 - T_0^4) + \alpha_{\text{conv}} (T_{\text{wall}} - T_0). \tag{6}$$

The subscripts "wall" and "0" denote the reactor wall and the surroundings, ϵ_{wall} is the emissivity of the reactor wall, and α_{conv} is the convective heat transfer coefficient from the reactor wall to the surroundings, which is derived from the following Nusselt correlation for a vertical cylinder [34].

$$Nu = \left\{0.825 + 0.387[Ra \cdot f_1(Pr)]^{1/6}\right\}^2 + 0.435\frac{h}{D} \tag{7}$$

$$f_1 = \left[1 + \left(\frac{0.492}{Pr}\right)^{9/16}\right]^{-16/9} \tag{8}$$

Due to the rotational symmetry of the cylinders, only a two-dimensional slice of the geometry is modeled and a symmetrical boundary condition is chosen at the center of the computational domain of the hot particle bed.

2.4. Material properties

The emissivity, thermal conductivity, specific heat capacity, and density of the reactor wall made from 3 mm Inconel 600 are taken from [35]. The emissivity of the Al_2O_3-SiO_2 insulation is from [36], its radiative extinction coefficient from [37], its effective thermal conductivity and density from [38], and its specific heat capacity from [39]. The emissivity of the ceria particles is taken from [36], the thermal conductivity from [40], the density from [41], and the specific heat capacity from [42]. The thermal conductivity of oxygen is from [43].

2.5. Numerical solution

The pseudo-transient continuation method is used to approximate the steady state of the heat exchanger in operation. The finite volume method is used for the spatial discretization of the energy conservation equations, subdividing the computational domain into a number of layers in radial and axial direction with constant properties at the cell centers. The energy conservation equations with two-dimensional heat transfer and temperature dependent thermal conductivities are then written for the whole computational domain giving a system of coupled non-linear equations. Using the boundary conditions shown above, the system of equations is solved for each time step with the implicit Euler method in Matlab. A grid convergence study is performed to determine the number of computational layers in the insulation and the reactive material. 100 layers in the radial direction are chosen for the particle beds, 10 for the insulation, and 120 in the axial direction in the baseline case.

3. Mixing of particle beds

There exists a critical time where the heat transfer from a wall to an adjacent particle bed changes from being dominated by the heat transfer from wall to bed surface (described by α_{ws}) to the one from bed surface to the bulk of the bed (described by α_{sb}, see Section 2.1.2, [31]). In the latter regime, a temperature gradient is developing in the particle bed as a function of time, which leads to a reduction of the heat transfer coefficient from bed surface to bulk α_{sb} and the overall heat transfer is deteriorated. A method to enhance overall heat transfer is mixing the beds of particles, which distributes the energy throughout the bed and leads to a more uniform temperature distribution. In case of perfect mixing, the bed assumes the caloric mean temperature in radial direction, the heat transfer coefficient from bed surface to bulk α_{sb} becomes infinite and the overall heat transfer is again described by α_{ws} (see Eq. (4)). In case the beds are not mixed, α_{sb} has a finite value, which defines the heat transfer. Depending on the implementation of the heat exchanger and therefore the level of mixing in the beds, the overall heat transfer coefficient will be between α_{sb} and α_{ws}, and the heat exchanger effectiveness will have an upper and a lower limit. In the following analysis, both limits are shown, where perfect mixing refers to mixing in the direction perpendicular to the movement of the beds. Active mixing of the particles may be achieved through the rotation of fins, by the introduction of gas streams, or by vibrations to the heat exchanger [44], while the particle elevation mechanism is likely to cause mixing of the particles, as well. In the case of perfect mixing, the bed assumes the radially averaged temperature. The energy input for lifting and mixing the particles is estimated to be small compared to the energy output of the produced syngas.

4. Results

The model introduced above is used to investigate the influence of different parameters on heat exchanger effectiveness defined in Eq. (9). The following parameters are investigated: reduction and oxidation temperatures (as entry temperatures into the heat exchanger), particle diameter, heat exchanger length, residence time, and radial dimensions of the particle beds. With the exception of entry temperatures, only a single parameter is varied while the others are kept constant according to the baseline case defined in the following.

4.1. Definition of heat exchanger effectiveness

The effectiveness of the heat exchanger is defined as the energy transferred to a certain mass of particles divided by the maximum energy that can possibly be recuperated. The heat exchanger effectiveness therefore describes the fraction of the total required thermal energy for cycling between the temperature levels of the chemical reactions that is recuperated by the heat exchanger. The transferred energy to the oxidized particles in the heat exchanger is found by integrating the (temperature dependent) heat capacity from the entry temperature $T_{\text{cold,in}} = T_{\text{L}}$ to the exit temperature $T_{\text{cold,out,j}}$ and multiplying with the respective mass

$$\varepsilon_{\text{he}} = \frac{\sum_1^{\text{j,end}} \dot{m}_{\text{j}} \int_{T_{\text{in,cold}}}^{T_{\text{out,cold,j}}} c_{\text{p}} \mathrm{d}T}{\dot{m} \int_{T_{\text{in,cold}}}^{T_{\text{in,hot}}} c_{\text{p}} \mathrm{d}T}, \tag{9}$$

where $\dot{m}_j$ is the mass flow rate and $T_{\mathrm{cold,out},j}$ is the temperature of the j-th annular section of the topmost layer of the cold bed, $\dot{m}$ is the total mass flow rate ecti, c_p is its specific heat capacity, and T_L and T_H are the temperatures of oxidation and reduction, respectively. In the baseline, the mass flow rate of particles is 0.01 kg s^{-1}.

4.2. Parameters for baseline case

The parameters for the baseline case are defined in Table 1.

The diameter of the cold particle bed is defined such that conservation of mass is fulfilled under the assumption of equal velocities of the hot and cold particle beds.

4.3. Entry temperatures into heat exchanger

The entry temperatures affect the heat exchanger effectiveness both by the altered temperature difference of the particle beds and the temperature dependence of thermal conductivities and heat transfer coefficients. In Fig. 2, the heat exchanger effectiveness is shown as a function of entry temperatures, T_L and T_H. For the case of no mixing of the beds, it rises from below 23% at T_H = 1500–1650 K to over 31% at T_L = 1200 K and T_H = 2000 K. If the beds are perfectly mixed, the effectiveness rises from 64% at T_H = 1500–1600 K to 78% at T_H = 1975–2000 K and T_L = 1075–1200 K. The enhancement through mixing is therefore significant, indicating that heat transfer in the beds is limiting. In general, η_{he} rises from the region of low entry temperatures to the region of high entry temperatures.

The overall heat transfer from the hot to the cold particle bed is defined by the temperature difference between the beds and by the resistances in the wall, in the particle beds and between particle beds and the wall, all of which are functions of temperature. For a non-insulating material, the resistance in the wall is comparably small and the main limitation for heat transfer is the resistance at the wall and in the beds. In case of mixing, the resistance in the bed is minimized and the limitation occurs at the surface between wall and beds, while in the case of unmixed beds the heat transfer in the beds is determining overall heat transfer. The heat exchanger effectiveness is therefore characterized by a trade-off between an increase of the difference of bed temperatures and an increase of the temperature dependent heat transfer coefficients. For the baseline case of the presented heat exchanger, effectiveness is maximized through an increase of the bed temperatures, which indicates that the enhancement of heat transfer coefficients in the beds and between the beds and the wall has a larger effect than the driving force of difference of bed temperatures.

Table 1
Parameters for basic configuration of particle heat exchanger.

Parameter	Label	Value	Unit
Cold side entry temperature	T_L	1000	K
Hot side entry temperature	T_H	1800	K
Temperature of surroundings	T_0	300	K
Pressure in heat exchanger (relative to standard state of 1 atm)	p_{red}	10^{-3}	atm
Total residence time in heat exchanger	t_{total}	360	s
Particle diameter	d	0.001	m
Heat exchanger length	h	0.5	m
Diameter of insulating centerpiece	$d_{bed,hot,i}$	0.04	m
Thickness of hot particle bed	$\Delta r_{bed,hot}$	0.01	m
Thickness of separation wall between particle beds	d_{sw}	0.003	m
Mass flow rate of ceria	$\dot{m}$	0.01	kg s^{-1}

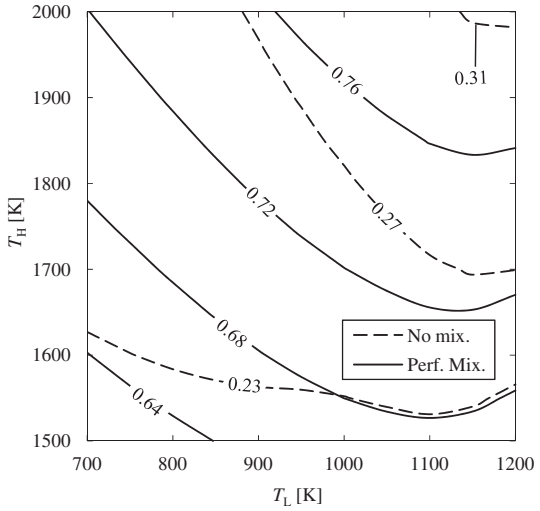

Fig. 2. Heat exchanger effectiveness as a function of reduction and oxidation temperatures T_H, T_L.

4.4. Particle diameter

The particle diameter has an influence on the total surface area of the reactive material but only slightly changes the porosity, as in Eq. (5) the ratio D/d is large and the porosity is close to the constant 0.375. Besides mechanical behavior and therefore transport properties, an altered diameter has an influence on the thermal transport within the particle beds and between the beds and the adjacent walls. According to Tsotsas [45], there exists a critical time at which the heat transfer between wall and adjacent particle bed changes from being dominated by heat transfer between wall and bed surface (described by α_{ws}) to heat transfer from the bed surface to the bulk (described by α_{sb}). Under the assumptions made for the baseline case, the critical time is on the order of seconds. Considering the total residence time in the heat exchanger, the main limitation to heat transfer between the unmixed beds is therefore expected from α_{sb} and therefore from the effective thermal conductivity of the beds. Assuming a moving packed bed, heat is transferred in the bed mainly through conduction (in the gas phase and solid phase) and radiation. At higher temperatures, radiation dominates the overall heat transfer within the bed [32,46]. As the radiative conductance term further depends on particle emissivity and diameter (Eq. (A.13)), larger particles are expected to enhance radiation and thus overall heat transfer. This is confirmed by experiments in the literature, e.g. by Chen and Churchill [46] who measured the effect of particle size on radiant conductivity of different materials such as glass, aluminum oxide, steel, and silicon carbide.

For perfect mixing, on the other hand, thermal conductivity in the beds approaches infinity and the heat transfer at the surface between the beds and the wall is limiting, which is deteriorated by an increase of particle size.

In Fig. 3, the particle diameter is varied from 10^{-6} m to 10^{-3} m to determine its influence on the heat exchanger effectiveness for the cases with no mixing and perfect mixing of the beds. Towards smaller sizes of the particles the tendency for the development of interlocking arches is increased, which may reduce the applicability for particle flow. These sizes are nevertheless included to demonstrate the influence on heat transfer. As expected, the heat exchanger effectiveness correlates positively with the particle diameter for the case of unmixed beds, rising from 3.5% at $d = 10^{-6}$ m to 26.7% at $d = 10^{-3}$ m. The relatively large increase in effectiveness is due to the enhancement of radiation heat transfer

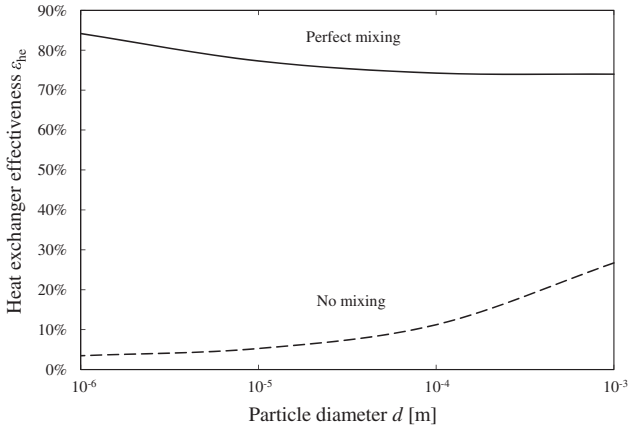

Fig. 3. Heat exchanger effectiveness as a function of particle diameter for the cases of no mixing and perfect mixing of the particle beds.

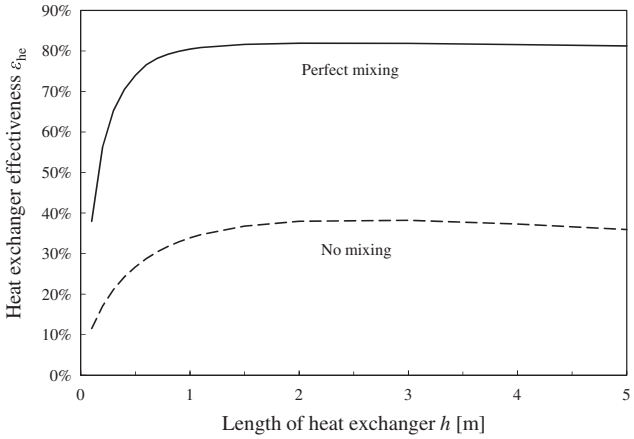

Fig. 4. Heat exchanger effectiveness for unmixed and perfectly mixed beds as a function of heat exchanger length.

in the beds. A requirement for this result is the high temperatures prevalent in the heat exchanger, which lead to the dominant radiation term. At lower temperature levels, the increase of particle diameter would thus have a lower influence on the heat exchanger effectiveness. For the case of perfect mixing, however, heat exchanger effectiveness falls from a value of 84% at $d = 10^{-6}$ m to 74% at $d = 10^{-3}$ m, as the heat exchange at the surface of wall and bed is inhibited by a growth of the particle diameter.

A larger particle diameter may on the other hand also have a negative influence on the operability of the solar reactor through a larger gas cross-over from the oxidation to the reduction zone: due to thermodynamics, oxidation is performed at atmospheric pressure and reduction at sub-atmospheric partial pressures of oxygen, which, in case of vacuum pumping, causes a pressure gradient over the particle beds. This pressure gradient leads to a constant gas stream from the oxidation to the reduction zone, which affects negatively the vacuum pumping power and the amount of oxidant required. An estimation of mass flow through the porous medium based on the Darcy law [47] shows that at particle diameters $d \leq 10^{-4}$ m, the bed represents an effective seal. Towards larger diameters, however, a technical solution may have to be found to reduce the loss of oxidant through the particle bed. One such solution has been suggested by a multi-stage pressure reduction in multiple reduction chambers [48].

4.5. Heat exchanger length

Under the conditions of the baseline case (Table 1) the axial length of the heat exchanger is varied to determine its influence on heat exchanger effectiveness. The mass flow rate of reactive material is kept constant, which gives a constant velocity of the beds. A prolongation of the axial length thus increases the total residence time of the particles in the heat exchanger and allows for a longer heat transfer period between hot and cold particles. In a regime where heat transfer is limited by heat diffusion in the reactive material, this could prove to be beneficial. However, if the length is chosen too large, losses to the environment become dominating. It is therefore expected that an optimal heat exchanger length exists, which will be shown in the following.

In Fig. 4, heat exchanger effectiveness is shown as a function of heat exchanger length between 0.1 m and 5 m for unmixed and perfectly mixed beds. For the former, effectiveness increases with length from 11.5% at 0.1 m up to 38.2% at 3 m, before it starts decreasing. If the beds are perfectly mixed, effectiveness shows a similar progression with a very steep increase from 0.1 m to 0.6 m, a long plateau, and maximum efficiencies exceeding 80%. The size of the plateau and the gradual decrease of effectiveness indicate that losses to the environment become significant only towards large heat exchanger lengths.

The optimum length and the achievable heat exchanger effectiveness depend on the chosen parameters of the system, e.g. the dimensions of the beds, the particle diameter, residence time, or temperatures entering the heat exchanger. The results shown in Fig. 4 are therefore strictly valid only for the chosen parameters and the assumed boundary conditions.

4.6. Residence time in heat exchanger

The residence time of the particles is varied at a constant length of the heat exchanger. On the one hand, longer residence times allow a longer heat exchange period between the hot and cold material. On the other hand, losses to the environment and due to axial heat transfer become more important for longer residence times. The optimal residence time is thus found as a trade-off between these two mechanisms.

Heat exchanger effectiveness is shown as a function of total residence time of the particles in the heat exchanger in Fig. 5. For unmixed beds, heat exchanger efficiencies rise up to 37.0% at a residence time of about 1500 s and decrease thereafter, while at perfectly mixed beds, the maximum of 79% occurs already at 725 s. The active mixing of the particle beds distributes the heat and eliminates the limitation by heat diffusion, which is seen in the case of unmixed beds. Therefore the maximum of effectiveness

Fig. 5. Heat exchanger effectiveness for unmixed and perfectly mixed beds as a function of total residence time in the heat exchanger.

is reached at a shorter residence time. If the optimum residence time is exceeded, effectiveness decreases due to losses to the surroundings by convection and radiation from the heat exchanger surface and due to axial heat transfer in the beds. In general, the solar power input to the reactor is directly coupled to the mass flow rate of reactive material and therefore to their residence time in the heat exchanger. This implies that the residence time can be used as a parameter to maximize effectiveness for a given heat exchanger geometry for a varying solar power input over the course of a day or for passing clouds.

4.7. Radial dimensions of heat exchanger

The radial thickness of the hot particle bed is varied between 0.002 m and 0.05 m, while the cold bed thickness is adjusted accordingly to conserve mass flux under the assumption of equal and constant bed speeds. The assumption of equal bed velocities is equivalent to equal residence times of the particles in the hot and cold section of the heat exchanger, respectively, which is 360 s in the baseline case (see Table 1). A change in bed diameters changes the bed volumes, which, at constant bed velocities, changes the mass flow rate of reactive material. At otherwise constant conditions of the reduction reaction, i.e. temperature and pressure, the solar power input is proportional to the mass flow. Increasing the diameter of the hot particle bed therefore requires a proportionally larger solar power input to retain the defined level of reduction of the material. In Fig. 6, the heat exchanger effectiveness is shown as a function of hot bed diameter. In case of unmixed beds, the maximum of effectiveness is reached for a reduction of the bed thickness towards the lowest value of 0.002 m, which is equivalent to two particle diameters in the baseline case. A limitation of Eq. (5) of $D/d > 2$ [33] precludes the calculation of even smaller bed geometries. As can be seen for the case of perfect mixing of the beds, effectiveness reaches a peak value close to the smallest bed diameter and decreases towards even smaller diameters because losses to the surroundings become significant. As the surface-to-volume ratio of a cylinder is inversely proportional to its radius, a decrease in radial dimensions will increase the relative weight of losses to the surroundings. Equivalently, it is expected that below the smallest analyzed bed thickness the effectiveness of the unmixed case decreases due to losses to the surroundings.

An increase of the radial dimensions of the particle beds leads to a decrease of heat exchanger effectiveness from a value of about 55% (no mixing) and 73% (perfect mixing) at $d_{\text{hot bed}} = 0.002$ m to 7% and 47% at $d_{\text{hot bed}} = 0.05$ m. The reason for the decrease in effectiveness is the addition of mass, which cannot be heated as efficiently. In case of the unmixed beds, the limitation occurs due to the thermal conductivity of the beds and in case of the perfectly mixed beds due to the heat transfer at the beds' surface. Mixing of the beds allows a significantly higher effectiveness because the heat transfer at the beds' surface is larger than in the beds.

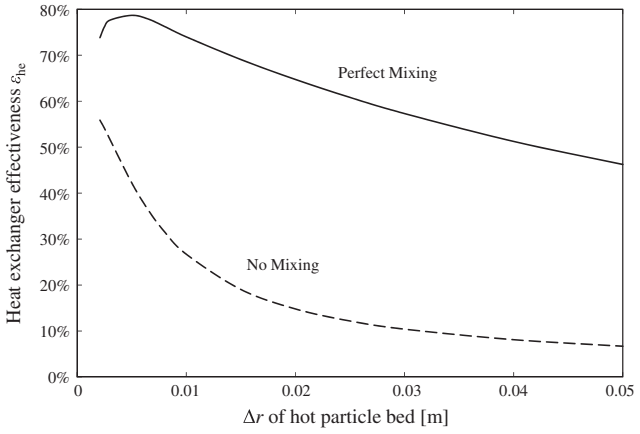

Fig. 6. Heat exchanger effectiveness for perfectly mixed and unmixed beds as a function of radial dimension of hot particle bed.

In order to reach high efficiencies in the heat exchanger, the dimensions of the particle beds in radial direction have to be chosen according to the length of the heat exchanger, the residence time of the particles, and their entry temperatures into the heat exchanger. Here, only the particle bed diameters were varied at otherwise constant conditions to study their influence on the heat exchange process. It is however possible to adjust the other parameters accordingly, especially residence time, to counterbalance the effect of additional mass in the heat exchanger. The magnitude and the location of the maximum effectiveness can therefore be shifted depending on the other system parameters.

5. Conclusions

For the production of syngas with solar thermochemical cycles, the implementation of heat recuperation is imperative for the achievement of higher efficiencies. Particle reactor concepts have been suggested due to several advantages such as higher flexibility and heating rates, resistivity to thermal shocks, or new heat recuperation concepts. This study presents a generic model of a particle heat exchanger for thermochemical cycles, where heat is transferred from a hot particle bed to a counter-flowing cold bed in a concentric double-walled geometry. The particles travel in moving beds, i.e. the reduced ones move downwards in the inner tube and the oxidized ones in counter-flow in the outer tube, where a solid wall ensures separation of the atmospheres. The model describes the heat exchange between the particle beds, where the conductivity of the beds and the heat transfer coefficients between the beds and the separating wall are expressed with established models in the literature. As the radial mixing of the beds has a significant influence on the heat exchange, both cases of radially unmixed and perfectly mixed beds (perpendicular to the bed movement) are analyzed, which gives a lower and an upper boundary for the heat exchanger performance.

From the variation of different parameters, recommendations for the heat exchanger design are deduced. An increase of the inlet temperatures leads to an enhanced heat transfer between the beds due to the improved heat transfer coefficients and thermal conductivities. The influence of the particle size depends on the mixing of the beds: a larger particle diameter reduces the heat transfer coefficient at the surface of the beds but increases the thermal conductivity through its radiative component. For unmixed beds, the main limitation to heat transfer occurs in the beds and thus a larger particle diameter enhances overall heat transfer. For perfectly mixed beds, the reduced heat transfer at the bed surface leads to a decreased overall performance. However, a larger particle diameter also increases the gas cross-over from the oxidation to the reduction chamber in case of vacuum pumping. Up to particle diameters of 10^{-4} m, the particle bed represents an effective seal, where for larger diameters technical solutions may be necessary to reduce the gas mass flow through the bed. The analysis of heat exchanger length, residence time of the particles in the heat exchanger, and radial dimensions of the beds shows that optimal values for each parameter can be found, which depend on the other system parameters. Heat exchanger eff over 50% are possible for unmixed beds and over 80% for perfectly mixed beds, given a favorable design of the device.

For the further development of two-step solar thermochemical cycles, heat exchangers are required to recuperate heat and thus to enhance effectiveness. With respect to the recently discussed

reactor concept of moving particles, the presented model serves as a valuable tool for the derivation of heat exchanger effectiveness and for its optimal design.

Acknowledgements

The authors gratefully acknowledge the contribution of Parthasarathy Pandi, Arne Roth and Valentin Batteiger. The research leading to these results has received funding from the European Union's Horizon 2020 research and innovation programme under grant agreement No 654408.

Appendix A. Governing equations

A fundamental characteristic of the thermal energy transfer from a wall to an adjacent bed of particles is a large temperature step between the wall and the first particles in the bed, and a further more moderate temperature gradient inside of the bed of particles. The heat exchange is therefore determined by (i) heat transfer at the boundary of the wall and the particle bed (described by the heat transfer coefficient α_{ws}) and (ii) heat transfer in the particle bed (α_{sb}). The heat transfer coefficient from the wall to the bed of particles α_{ws} is comprised of the contributions for heat transfer between wall and a single particle, between wall and gas phase, by radiation, and by direct contact between the wall and the particles.

$$\alpha_{ws} = \Phi_A \alpha_{wp} + (1-\Phi_A)\frac{2\lambda_G/d}{\sqrt{2}+(2l+2\delta)/d} + \alpha_{rad} + \alpha_{dir} \tag{A.1}$$

Φ_A is the plate surface coverage factor of the particles, α_{wp} is the heat transfer coefficient between the wall and a particle, λ_G is the continuum heat conductivity of the gas, d is the particle diameter, l is the modified mean free path of the gas molecules, δ is the roughness factor of the particles, α_{rad} is the heat transfer coefficient for radiation, and α_{dir} is the heat transfer coefficient for direct contact of particle and wall.

α_{wp} is defined as

$$\alpha_{wp} = \frac{4\lambda_G}{d}\left[\left(1+\frac{2l+2\delta}{d}\right)\ln\left(1+\frac{d}{2l+2\delta}\right)-1\right], \tag{A.2}$$

where the modified mean free path l is

$$l = 2\Lambda\frac{2-\gamma}{\gamma}. \tag{A.3}$$

Λ is the mean free path and is derived from

$$\Lambda = \frac{16}{5}\sqrt{\frac{\mathcal{R}T}{2\pi M}}\frac{\eta_{vis}}{p}, \tag{A.4}$$

where $\mathcal{R}$ is the ideal gas constant, M is the molecular mass of the gas, T its temperature, η_{vis} its dynamic viscosity, and p its pressure. γ is the accommodation coefficient, which is derived with

$$\log\left(\frac{1}{\gamma}-1\right) = 0.6 - \frac{(1000\mathrm{K/T})+1}{C}, \tag{A.5}$$

where C is 2.8 for air and this value is also chosen for oxygen due to lack of experimental data [49–51].The radiative heat transfer coefficient is

$$\alpha_{rad} = 4\sigma\frac{1}{\frac{1}{\varepsilon_{wall}}+\frac{1}{\varepsilon_{bed}}-1}T^3, \tag{A.6}$$

where σ is the Stefan-Boltzmann constant, ε_{wall} is the emissivity of the wall, and ε_{bed} is the emissivity of the bed of particles.

The contribution from the direct contact of particles and wall is

$$\alpha_{dir} = 2\frac{a}{d}\frac{\lambda_S}{d}, \tag{A.7}$$

where a is the diameter of the contact surface area of particle and wall in case the particles are not perfectly spherical, d is the particle diameter, and λ_s is the thermal conductivity of the particles. For the ratio a/d, a value of 3×10^{-4} is chosen [31].

Assuming a constant wall temperature and a moving bed of particles, the time averaged heat transfer coefficient for the penetration of heat from the bed surface into the bulk is expressed after [31] with

$$\alpha_{sb} = \frac{2}{\pi}\frac{\sqrt{(\rho c_p \lambda)_{bed}}}{\sqrt{t}}, \tag{A.8}$$

with the density ρ, the heat capacity c_p and the thermal conductivity λ, each referring to the bed of particles and evaluated at the mean bed temperature, and the contact time t. Here, for simplification, the arithmetic mean temperature of the bed is chosen instead of the calorific mean temperature. For a moving bed and an isothermal wall, the contact time is equal to the total residence time of the particles on the wall L/v, with the length of the wall L and the velocity of the particles v. However, for the case of the double-walled heat exchanger, the wall cannot be assumed to be isothermal and a different contact time has to be used. When the cold bed enters the heat exchanger, the particles have a uniform temperature of T_L, which increases while the particles rise, until it reaches its final temperature at the exit of the heat exchanger. When the bed is isothermal, $\alpha_{sb}\to\infty$ and the overall heat transfer coefficient is equal to α_{ws} (see Eq. (4)) [31]. After a critical time, $\alpha_{sb} < \alpha_{ws}$, and the heat transfer is limited by the resistance from bed surface to the bulk material of the bed. For both hot and cold beds, the overall heat transfer coefficient α will therefore have a high value of α_{ws} at the entrance of the heat exchanger ($t\approx0$), which drops to lower values along the axial length ($t > t_{crit}$). As the particles in each of the beds move with the same velocity along the wall, the contact time between particle beds and wall is therefore chosen such that $t = m\times\Delta t^{num}$, where Δt^{num} is the residence time of the particles in each of the numerical layers and m is the index of the layers. As the time averaged expression for the heat transfer coefficient is used instead of the unknown momentary value, a slight inaccuracy is introduced, however the deviation between the values is very small [31].

The thermal conductivity of the particle bed is expressed with

$$\frac{\lambda_{bed}}{\lambda_f} = (1-\sqrt{1-\varphi})\varphi[(\varphi-1+k_G^{-1})^{-1}+k_{rad}] + \sqrt{1-\varphi} \times[\psi k_p + (1-\psi)k_c]. \tag{A.9}$$

λ_{bed} is the thermal conductivity of the bed of particles, λ_f that of the fluid in-between the particles, φ is the porosity of the bed, ψ is the flatness coefficient of the particles, and k_G, k_{rad} and k_c are the thermal conductivity of the gas including the effect of pressure dependence, the radiative conductivity, and the thermal conductivity of the core of the unit cell, each relative to the fluid thermal conductivity. The pressure dependence of the particle bed is included, which reflects the decrease of thermal conductivity with pressure according to the Smoluchowski effect [32].

$$k_c = \frac{2}{N}\left\{\frac{B(k_p+k_{rad}-1)}{N^2k_Gk_p}\ln\frac{k_p+k_{rad}}{B[k_G+(1-k_G)(k_p+k_{rad})]} + \frac{B+1}{2B}\left[\frac{k_{rad}}{k_G}-B\left(1+\frac{1-k_G}{k_G}k_{rad}\right)\right]-\frac{B-1}{Nk_G}\right\}, \tag{A.10}$$

with

$$N = \frac{1}{k_G}\left(1+\frac{k_{rad}-Bk_G}{k_p}\right)-B\left(\frac{1}{k_G}-1\right)\left(1+\frac{k_{rad}}{k_p}\right), \tag{A.11}$$

$$B = C_f \left[\frac{(1-\varphi)}{\varphi}\right]^{\frac{10}{9}}, \tag{A.12}$$

$$k_{rad} = \frac{\lambda_{rad}}{\lambda_f} = \frac{4\sigma}{(2/\varepsilon)-1} T^3 \frac{d}{\lambda_f}, \tag{A.13}$$

$$k_G = \frac{\lambda_G}{\lambda_f} = \left[1 + \left(\frac{l}{d}\right)\right]^{-1}, \tag{A.14}$$

$$k_p = \frac{\lambda_p}{\lambda_f}. \tag{A.15}$$

l is the modified mean free path of the gas molecules and is calculated after Eq. (A.3), d is the particle diameter, ε is the particle emissivity, φ is the porosity of the bed, C_f is the form factor of the particles, which has to be determined experimentally and which is 1.25 for spherical particles [32], and k_p is the thermal conductivity of the particles relative to the fluid conductivity.

Eqs. (A.10)–(A.15) are then used in Eq. (A.9) to derive the thermal conductivity of the particle bed.

Appendix B. Comparison of model with experimental data

In order to demonstrate the validity of the chosen approach of modeling the heat transfer between moving beds of particles, partial results of the model are compared to experimental results in the literature for the thermal conductivity of the particle bed λ_{bed}, the overall heat transfer coefficient between wall and bed of particles α [31], and steady-state temperature profiles of a packed bed of particles contained in a double-walled tubular geometry [52]. Results from the model compare well with the literature data, where an exemplary result is shown in the following for the temperature distribution in a particle bed.

In order to allow the comparison of heat transfer coefficients and thermal conductivity of the bed at the same time, the experiment described in [52] is modeled and experimental and theoretical values are compared.

In [52], a packed bed of glass beads is used, which is contained between a stainless steel tube and a Carborundum electric heater held in a coaxial silica tube.

In Fig. A1, the modeled temperatures are compared with the experimental data from [52]. The general temperature progression in the particle bed is predicted correctly by the model. In the experiments, the functional dependence of temperature on particle diameter is slightly stronger, however, in the model the trend of decreasing temperatures with smaller particles is captured correctly. The authors state that a steady state is reached in the experiment without giving the exact contact time, where, in the model, a contact time of 3000 s between the particle bed and the surrounding walls is found to represent the results best. An insulation thickness of 1 cm is chosen as the exact value could not be found in the description of the experiment. The density and the specific heat capacity of the fire brick insulation is taken from [53] and its thermal conductivity from [29]. The effective density of the bed is taken to be 1500 kg m^{-3} [54]. Considering that not all of the experimental conditions and material properties are known, the results from the computational model match well with the experimental data in [52].

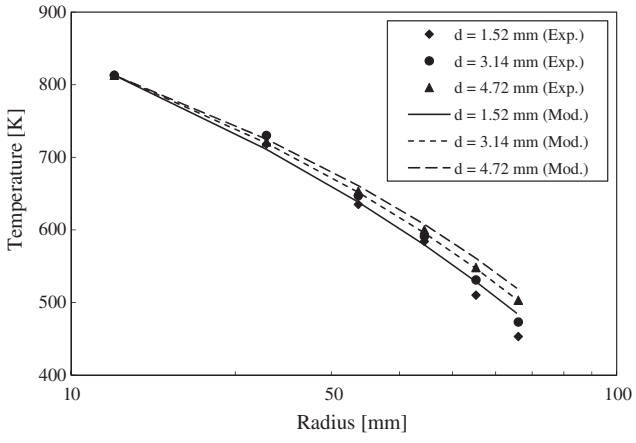

Fig. A1. Comparison of modeled and experimental temperatures of a particle bed in a double-walled tube with a heated inner section. Experimental values are from [52]. The difference of the computational and experimental values is partly explained by deviating material properties and unknown experimental conditions, which could not fully be represented by the model.

References

[1] D.A. Marxer, P. Furler, J.R. Scheffe, H. Geerlings, C. Falter, V. Batteiger, A. Sizmann, A. Steinfeld, Demonstration of the entire production chain to renewable kerosene via solar-thermochemical splitting of H_2O and CO_2, Energy Fuels 29 (2015) 3241–3250, https://doi.org/10.1021/acs.energyfuels.5b00351.

[2] E.B. Stechel, J.E. Miller, Re-energizing CO_2 to fuels with the sun: issues of efficiency, scale, and economics, J. CO_2 Util. 1 (2013) 28–36, https://doi.org/10.1016/j.jcou.2013.03.008.

[3] W.C. Chueh, C. Falter, M. Abbott, D. Scipio, P. Furler, S.M. Haile, A. Steinfeld, High-flux solar-driven thermochemical dissociation of CO_2 and H_2O using nonstoichiometric ceria, Science 330 (2010) 1797–1801, https://doi.org/10.1126/science.1197834.

[4] B.J. Hathaway, R. Bala Chandran, A.C. Gladen, T.R. Chase, J.H. Davidson, Demonstration of a solar reactor for carbon dioxide splitting via the isothermal ceria redox cycle and practical implications, Energy Fuels 30 (2016) 6654–6661, https://doi.org/10.1021/acs.energyfuels.6b01265.

[5] A. Banerjee, R. Bala Chandran, J.H. Davidson, Experimental investigation of a reticulated porous alumina heat exchanger for high temperature gas heat recovery, Appl. Therm. Eng. 75 (2015) 889–895, https://doi.org/10.1016/j.applthermaleng.2014.10.033.

[6] J.E. Miller, M.A. Allendorf, A. Ambrosini, E.N. Coker, R.B. Diver, I. Ermanoski, L.R. Evans, R.E. Hogan, A.H. Mcdaniel, Development and assessment of solar-thermal-activated fuel production: phase 1 summary, Sandia Rep. (2012) 1–38.

[7] D. Marxer, P. Furler, M. Takacs, A. Steinfeld, Solar thermochemical splitting of CO_2 into separate streams of CO and O_2 with high selectivity, stability, conversion, and efficiency, Energy Environ. Sci. 10 (2017) 1142–1149, https://doi.org/10.1039/C6EE03776C.

[8] J. Lapp, J.H. Davidson, W. Lipiński, Efficiency of two-step solar thermochemical non-stoichiometric redox cycles withheat recovery, Energy 37 (2012) 591–600, https://doi.org/10.1016/j.energy.2011.10.045.

[9] C.P. Falter, A. Sizmann, R. Pitz-Paal, Modular reactor model for the solar thermochemical production of syngas incorporating counter-flow solid heat exchange, Sol. Energy 122 (2015) 1296–1308, https://doi.org/10.1016/j.solener.2015.10.042.

[10] R.B. Diver, J.E. Miller, M.D. Allendorf, N.P. Siegel, R.E. Hogan, Solar thermochemical water-splitting ferrite-cycle heat engines, J. Sol. Energy Eng. 130 (2008) 041001, https://doi.org/10.1115/1.2969781.

[11] J. Lapp, J.H. Davidson, W. Lipiński, Heat transfer analysis of a solid-solid heat recuperation system for solar-driven nonstoichiometric cycles, J. Sol. Energy Eng. 135 (2013) 031004, https://doi.org/10.1115/1.4023357.

[12] J. Felinks, S. Brendelberger, M. Roeb, C. Sattler, R. Pitz-paal, Heat recovery concept for thermochemical processes using a solid heat transfer medium, Appl. Therm. Eng. 73 (2014) 1004–1011, https://doi.org/10.1016/j.applthermaleng.2014.08.036.

[13] I. Ermanoski, N.P. Siegel, E.B. Stechel, A new reactor concept for efficient solar-thermochemical fuel production, J. Sol. Energy Eng. 135 (2013) 031002, https://doi.org/10.1115/1.4023356.

[14] R.B. Chandran, R.M. De Smith, J.H. Davidson, Model of an integrated solar thermochemical reactor/reticulated ceramic foam heat exchanger for gas-phase heat recovery, Int. J. Heat Mass Transf. 81 (2015) 404–414.

[15] J.E. Miller, A. Ambrosini, S.M. Babiniec, E.N. Coker, C.K. Ho, H. Al-Ansary, S.M. Jeter, P.G. Loutzenhiser, N.G. Johnson, E.B. Stechel, High performance reduction/oxidation metal oxides for thermochemical energy storage (PROMOTES), in: Vol. 1 Biofuels, Hydrog. Syngas, Altern. Fuels; CHP Hybrid Power Energy Syst. Conc. Sol. Power; Energy Storage; Environ. Econ. Policy Considerations Adv. Energy Syst. Geothermal, Ocean. Emerg. E, ASME, 2016, pp. V001T04A024. http://doi.org/10.1115/ES2016-59660.

[16] P. Furler, J. Scheffe, M. Gorbar, L. Moes, U. Vogt, A. Steinfeld, Solar thermochemical CO_2 splitting utilizing a reticulated porous ceria redox system, Energy Fuels 26 (2012) 7051–7059, https://doi.org/10.1021/ef3013757.

[17] J.R. Scheffe, M. Welte, A. Steinfeld, Thermal reduction of ceria within an aerosol reactor for H_2O and CO_2 splitting, Ind. Eng. Chem. Res. 53 (2014) 2175–2182, https://doi.org/10.1021/ie402620k.
[18] S. Brendelberger, C. Sattler, Concept analysis of an indirect particle-based redox process for solar-driven H_2O/CO_2 splitting, Sol. Energy 113 (2015) 158–170, https://doi.org/10.1016/j.solener.2014.12.035.
[19] C. Ho, J. Christian, D. Gill, A. Moya, S. Jeter, S. Abdel-Khalik, D. Sadowski, N. Siegel, H. Al-Ansary, L. Amsbeck, B. Gobereit, R. Buck, Technology advancements for next generation falling particle receivers, Energy Procedia 49 (2013) 398–407, https://doi.org/10.1016/j.egypro.2014.03.043.
[20] C.K. Ho, A review of high-temperature particle receivers for concentrating solar power, Appl. Therm. Eng. 109 (2016) 958–969, https://doi.org/10.1016/j.applthermaleng.2016.04.103.
[21] L.O. Schunk, P. Haeberling, S. Wepf, D. Wuillemin, A. Meier, A. Steinfeld, A receiver-reactor for the solar thermal dissociation of zinc oxide, J. Sol. Energy Eng. ASME 130 (2008), https://doi.org/10.1115/1.2840576.
[22] G. Maag, G. Zanganeh, A. Steinfeld, Solar thermal cracking of methane in a particle-flow reactor for the co-production of hydrogen and carbon, Int. J. Hydrogen Energy 34 (2009) 7676–7685, https://doi.org/10.1016/j.ijhydene.2009.07.037.
[23] N. Gokon, S. Takahashi, H. Yamamoto, T. Kodama, Thermochemical two-step water-splitting reactor with internally circulating fluidized bed for thermal reduction of ferrite particles, Int. J. Hydrogen Energy 33 (2008) 2189–2199, https://doi.org/10.1016/j.ijhydene.2008.02.044.
[24] S.M. Babiniec, J.E. Miller, A. Ambrosini, E. Stechel, E.N. Coker, P.G. Loutzenhiser, C.K. Ho, Considerations for the design of a high-temperature particle reoxidation reactor for extraction of heat in thermochemical energy storage systems, in: Vol. 1 Biofuels, Hydrog. Syngas, Altern. Fuels; CHP Hybrid Power Energy Syst. Conc. Sol. Power; Energy Storage; Environ. Econ. Policy Considerations Adv. Energy Syst. Geothermal, Ocean. Emerg. E, ASME, 2016, pp. V001T04A021. http://doi.org/10.1115/ES2016-59646.
[25] V.V. Zedtwitz-Nikulshyna, CO_2 capture from atmospheric air via solar driven carbonation-calcination cycles, Dissertation, ETH Zurich, 2009.
[26] I. Ermanoski, A. Orozco, C2R2: Compact Compound Recirculator/Recuperator for Renewable Energy and Energy Efficient Thermochemical Processing, SANDIA Report, SAND2015-7320, 2015, pp. 1–46.
[27] A. Mcdaniel, I. Ermanoski, DOE Hydrogen and Fuel Cells Program: FY 2015 Annual Report: High Efficiency Solar Thermochemical Reactor for Hydrogen Production, 2015
[28] C.P. Falter, R. Pitz-Paal, A generic solar-thermochemical reactor model with internal heat diffusion for counter-flow solid heat exchange, Sol. Energy 144 (2017) 569–579, https://doi.org/10.1016/j.solener.2017.01.063.
[29] S. Yagi, D. Kunii, Studies on effective thermal conductivities in packed beds, AIChE J. 3 (1957) 373–381, https://doi.org/10.1002/aic.690030317.
[30] J.R. Howell, R. Siegel, M. Mengüc, R. Pinar, Thermal Radiation Heat Transfer, CRC Press, Boca Raton, 2011.
[31] E. Schlünder, Heat transfer to packed and stirred beds from the surface of immersed bodies, Chem. Eng. Process. Process Intensif. 18 (1984) 31–53, https://doi.org/10.1016/0255-2701(84)85007-2.
[32] C. Ullrich, T. Bodmer, VDI-Wärmeatlas, D6 Stoffwerte von Feststoffen, Springer, Berlin Heidelberg, Berlin, Heidelberg, 2013.
[33] A.S. Pushnov, Calculation of average bed porosity, Chem. Pet. Eng. 42 (2006) 14–17, https://doi.org/10.1007/s10556-006-0045-x.
[34] H. Klan, VDI-Wärmeatlas, Springer, Berlin Heidelberg, Berlin, Heidelberg, 2013.
[35] Special Metals, Inconel Alloy 600, 2015. www.specialmetals.com/documents/Inconel alloy 600.pdf (accessed June 1, 2015).
[36] Y.S. Touloukian, D.P. DeWitt, Thermophysical Properties of Matter – The TPRC Data Series – Vol.8 Thermal Radiative Properties – Nonmetallic Solids, CINDAS/Purdue University, 1972.
[37] B. Zhang, S. Zhao, X. He, S. Du, High temperature thermal physical properties of high-alumina fibrous insulation, J. Mater. Sci. Technol. 23 (2007) 860–864.
[38] Zircar Zirconia, Fibrous Insulation – Type Buster M35, 2015. http://www.zircarzirconia.com/product-literature/buster.php (accessed January 1, 2015).
[39] P. Furler, Solar thermochemical CO_2 and H_2O splitting via ceria redox reactions, Dissertation, ETH Zürich, 2014. http://doi.org/10.3929/ethz-a-010207593.
[40] Y.S. Touloukian, R.W. Powell, C.Y. Ho, P.G. Klemens, Thermophysical Properties of Matter – The TPRC Data Series – Vol. 2. Thermal Conductivity – Nonmetallic Solids, CINDAS/Purdue University, 1971.
[41] U.S. Environmental Protection Agency, Toxicological Review Cerium Oxide and Cerium Compounds, 2009.
[42] I. Riess, M. Ricken, J. Noelting, Specific heat of non-stoichiometric ceria (CeO_y), Solid State Ionics 18–19 (1986) 725–726, https://doi.org/10.1016/0167-2738(86)90250-X.
[43] M. Kleiber, R. Joh, VDI-Wärmeatlas, Kapitel D, 2013.
[44] W.H.P. Tomas, Powder mixing and blending; Fluid flow through particle beds, Universität Magdeburg, Course documentation, 2014.
[45] E. Tsotsas, VDI-Wärmeatlas, Springer, Berlin Heidelberg, Berlin, Heidelberg, 2013.
[46] J.C. Chen, S.W. Churchill, Radiant heat transfer in packed beds, AIChE J. 9 (1963) 35–41, https://doi.org/10.1002/aic.690090108.
[47] H. Darcy, Les fontaines publiques de la ville de Dijon: exposition et application des principes à suivre et des formules à employer dans les questions de distribution d'eau, Paris, 1856. <http://scholar.google.com/scholar?hl=en&btnG=Search&q=intitle:Les+fontaines+publiques+de+la+ville+de+dijon#0>.
[48] I. Ermanoski, A. Orozco, J. Grobbel, Pressure separation and gas flows in a prototype vacuum-pumped solar-thermochemical reactor, AIP Conf. Proc. 1850 (2017), https://doi.org/10.1063/1.4984461.
[49] H. Martin, T. Verfahrenstechnik, K. Institut, VDI-Wärmeatlas, Springer, Berlin Heidelberg, Berlin, Heidelberg, 2013.
[50] M. Heyde, H.-J. Klocke, Wärmeübergang zwischen Wirbelschicht und Einbauten – ein Problem des Wärmeübergangs bei kurzfristigem Kontakt, Chemie Ing. Tech. 51 (1979) 318–319, https://doi.org/10.1002/cite.330510417.
[51] H. Martin, Wärme- und Stoffübertragung in der Wirbelschicht, Chemie Ing. Tech. 52 (1980) 199–209, https://doi.org/10.1002/cite.330520303.
[52] N. Wakao, K. Kato, Effective thermal conductivity of packed beds, J. Chem. Eng. Jpn. 2 (1969) 24–33. http://scholar.google.com/scholar?hl=en&btnG=Search&q=intitle:EFFECTIVE+THERMAL+CONDUCTIVITY+OF+PACKED+BEDS#0.
[53] Mantec Technical Ceramics, Ultralite Insulating Firebricks – Technical Data Sheet, 2016. <http://www.mantectechnicalceramics.com/sites/default/files/uifb_technical_data_sheet_june_2016_v5.pdf>.
[54] N.K. Harakas, K. Beatty, Moving bed heat transfer: I effect of interstitial gas with fine particles, Chem. Eng. Symp. Ser. 59 (1963) 122–128.